5176 *Chem. Mater.* **2009,** *21,* 5176–5186
DOI:10.1021/cm9021084

CHEMISTRY OF MATERIALS
Article

Structure and Properties of Multiferroic Oxygen Hyperstoichiometric $BiFe_{1-x}Mn_xO_{3+\delta}$

Sverre M. Selbach,[†] Thomas Tybell,[‡] Mari-Ann Einarsrud,[†] and Tor Grande*[,†]

[†]*Department of Materials Science and Engineering, Norwegian University of Science and Technology, 7491 Trondheim, Norway, and* [‡]*Department of Electronics and Telecommunications, Norwegian University of Science and Technology, 7491 Trondheim, Norway*

Received July 13, 2009. Revised Manuscript Received September 23, 2009

The structure and properties of materials in the $BiFeO_3$-rich side of the pseudo-binary phase diagram $BiFeO_3-BiMnO_3$ are reported. Manganese substitution (x) and oxygen hyperstoichiometry (δ) are demonstrated to strongly affect the crystallographic properties, electrical conductivity, and phase-transition temperatures of $BiFe_{1-x}Mn_xO_{3+\delta}$. Increasing the manganese content and oxygen hyperstoichiometry of the materials depresses the Néel temperature, the ferroelectric Curie temperature, and the transition temperature from the paraelectric, ferroelastic structure to the paraelastic, cubic perovskite structure. The thermodynamics of the ambient pressure solid solubility is discussed and a phase diagram for the system $BiFe_{1-x}Mn_xO_{3+\delta}$ is presented, establishing the stability regions of three, two, one, and zero simultaneous ferroic properties. Finally, technological implications of the influence of manganese and excess oxygen are discussed.

Introduction

Materials possessing two or more of the ferroic properties ferroelasticity, ferroelectricity, and (anti)ferromagnetism are known as being multiferroic.[1] One interesting possibility is coupling between different ferroic order parameters, e.g., ferroelectric and magnetic ordering can be coupled through the magnetoelectric effect.[2] Because of their potential technological applications in multiferroelectric memories, sensors, and spintronics, they have become the subject of intense research.[3] $BiFeO_3$ is the most widely studied multiferroic material and exhibits room-temperature multiferroism with a high Néel temperature (T_N) of 370 °C and a ferroelectric Curie temperature of 820−830 °C.[1,4,5] The ground state of bulk $BiFeO_3$ is a rhombohedrally distorted perovskite belonging to the polar space group $R3c$ with lattice parameters $a_h = 5.58$ Å and $c_h = 13.87$ Å in the hexagonal setting.[6] A large spontaneous polarization of 50−60 $\mu C/cm^2$ has been reported for epitaxial thin films, high-quality single crystals, and polycrystalline ceramics.[7] The antiferromagnetic ordering in bulk $BiFeO_3$ is G-type below T_N,[7] and a canted spin structure gives a spiral modulation with a periodicity of 62 nm, incommensurate with the crystal lattice.[8]

Although several different crystal structures have recently been proposed for the paraelectric polymorph,[9−12] the most compelling experimental evidence from a neutron powder diffraction study by Arnold et al. suggests a $GdFeO_3$-type orthorhombic structure with space group $Pbnm$.[13] A second structural transition, to the ideal cubic perovskite structure at 925 ± 5 °C, has also been reported

*To whom correspondence should be addressed. E-mail: tor.grande@material.ntnu.no.

(1) (a) Smolenskii, G. A.; Chupis, I. E. *Sov. Phys. Usp.* **1982**, *25*, 475. (b) Eerenstein, W.; Mathur, N. D.; Scott, J. F. *Nature* **2006**, *442*, 759.
(2) (a) Fiebig, M.; Lottermoser, Th.; Fröhlich, D.; Goltsec, A. V.; Pisarev, R. V. *Nature* **2002**, *419*, 818. (b) Fiebig, M. *J. Phys. D: Appl. Phys.* **2005**, *38*, R123.
(3) Ramesh, R.; Spaldin, N. A. *Nat. Mater.* **2007**, *6*, 21.
(4) Teague, J. R.; Gerson, R.; James, W. J. *Solid State Commun.* **1970**, *8*, 1073.
(5) Kisilev, S. V.; Ozerov, R. P.; Zhdanov, G. S. *Sov. Phys. Dokl.* **1963**, *7*, 742.
(6) (a) Moreau, J. M.; Michel, C.; Gerson, R.; James, W. J. *J. Phys. Chem. Solids* **1971**, *32*, 1315. (b) Kubel, F.; Schmid, H. *Acta Crystallogr., Sect. B: Struct. Sci.* **1990**, *46*, 698.
(7) (a) Wang, J.; Neaton, J. B.; Zheng, H.; Nagarajan, V.; Ogale, S. B.; Liu, B.; Viehland, D.; Vaithyanathan, V.; Schlom, D. G.; Waghmare, U. V.; Spaldin, N. A.; Rabe, K. M.; Wuttig, M.; Ramesh, R. *Science* **2003**, *299*, 1719. (b) Lebeugle, D.; Colson, D.; Forget, A.; Viret, M.; Bonville, P.; Marucco, J. F.; Fusil, S. *Phys. Rev. B* **2007**, *76*, 024116. (c) Shvartsman, V. V.; Kleemann, W.; Haumont, R.; Kreisel, J. *Appl. Phys. Lett.* **2007**, *90*, 172115.
(8) Sosnowska, I.; Peterlin-Neumaier, T.; Steichele, E. *J. Phys. C: Solid State Phys.* **1982**, *15*, 4835.
(9) Kornev, I. A.; Lisenkov, S.; Haumont, R.; Dkhil, B.; Bellaiche, L. *Phys. Rev. Lett.* **2007**, *99*, 227602.
(10) Palai, R.; Katiyar, R. S.; Schmid, H.; Tissot, P.; Clark, S. J.; Robertson, J.; Redfern, S. A. T.; Catalan, G.; Scott, J. F. *Phys. Rev. B* **2008**, *77*, 014110.
(11) Haumont, R.; Kornev, I. A.; Lisenkov, S.; Bellaiche, L.; Kreisel, J.; Dkhil, B. *Phys Rev. B* **2008**, *78*, 134108.
(12) Selbach, S. M.; Tybell, T.; Einarsrud, M.-A.; Grande, T. *Adv. Mater.* **2008**, *20*, 3692.
(13) Arnold, D. C.; Knight, K. S.; Morrison, F. D.; Lightfoot, P. *Phys. Rev. Lett.* **2009**, *102*, 027602.
(14) Selbach, S. M.; Tybell, T.; Einarsrud, M.-A.; Grande, T. *Phys. Rev. B* **2009**, *79*, 214113.
(15) (a) Atou, T.; Chiba, H.; Ohoyama, K.; Tamaguchi, Y.; Syono, Y. *J. Solid State Chem.* **1999**, *145*, 639. (b) Moreira dos Santos, A.; Parashar, S.; Raju, A. R.; Zhao, Y. S.; Cheetham, A. K.; Rao, C. N. R. *Solid State Commun.* **2002**, *122*, 49. (c) Belik, A. A.; Iikubo, S.; Yokosawa, T.; Kodama, K.; Igawa, N.; Shamoto, S.; Azuma, M.; Takano, M.; Kimoto, K.; Matsui, Y.; Takayama-Muromachi, E. *J. Am. Chem. Soc.* **2007**, *129*, 971. (d) Baettig, P.; Seshadri, R.; Spaldin, N. A. *J. Am. Chem. Soc.* **2007**, *129*, 9854. (e) Montanari, E.; Calestani, G.; Righi, L.; Giliolo, E.; Bolzoni, F.; Knight, K. S.; Radaelli, P. G. *Phys. Rev. B* **2007**, *75*, 220101(R).

 Published on Web 10/14/2009

for $BiFeO_3$.[10] An intermediate, paraelectric polymorph with space group *Pbnm* was also found for $BiFe_{0.7}Mn_{0.3}O_{3+\delta}$;[14] thus, the most probable structural phase-transition sequence of $BiFeO_3$ is $R3c \leftrightarrow Pbnm \leftrightarrow Pm\bar{3}m$. $BiMnO_3$ is also termed a multiferroic material, although it has been debated whether it is polar or antipolar.[15] Oxygen nonstoichiometry has only recently been systematically quantified and shown to change the crystal symmetry and magnetic properties of $BiMnO_3$;[16] however, it has also been reported to influence the high-temperature behavior.[17] Manganese is known to readily adopt the oxidation states of 3+ and 4+ in perovskites, e.g., in $LaMnO_{3+\delta}$.[18,19] However, the oxygen nonstoichiometry in pure $BiFeO_{3\pm\delta}$ is <0.01 at 800 °C.[20] Manganese is a particularly interesting element for substitution, because of reports of enhanced multiferroic properties in $BiFe_{1-x}Mn_xO_3$.[21−23] Mn substitution does not alter the space group of $BiFeO_3$ for $x \leq 0.3$;[21,22] thus, the multiferroic properties can be tailored by the manganese content. High pressure is necessary to form phase-pure perovskite for $x > 0.3$.[24] Here, we report the influence of oxygen hyperstoichiometry and Mn substitution in the iron-rich side of the $BiFeO_3-BiMnO_3$ pseudobinary system. We quantify the influence of Mn substitution and oxygen hyperstoichiometry on the structural properties, phase-transition temperatures, and electrical conductivity. Implications for device applications are discussed, and a phase diagram is established.

Experimental Section

Synthesis and Thermogravimetry. $BiFe_{1-x}Mn_xO_{3+\delta}$ was prepared via solid-state reaction between dried Bi_2O_3 (Aldrich, >99.9%), Fe_2O_3 (Sigma−Aldrich, 99.98%) and Mn_2O_3 (prepared from Riedel-de-Haën, $Mn(CH_3COO)_2 \cdot 4H_2O$, >99.5%, by annealing in air at 700 °C for 8 h). Pellets of stoichiometric binary oxide mixtures were pressed and immersed in sacrificial powder before firing. Samples in the following were fired in air for 6 min at 900 °C and subsequently quenched in air (labeled as "q") or cooled in air with a rate of 400 °C h^{-1} (labeled as "c"). One sample with $x = 0.3$ was fired in flowing 5.0 N_2 for 30 min at 850 °C to reduce Mn^{4+} to Mn^{3+}.

Thermogravimetry to determine oxygen nonstoichiometry (δ in $BiFe_{0.7}Mn_{0.3}O_{3+\delta}$) was performed on three parallels of fine-crushed powders by annealing for 30 min at 850 °C in flowing 5.0 N_2 to reduce manganese to the trivalent oxidation state (Mn^{3+}). It is assumed that the content of Mn^{4+} is negligible under these conditions, corresponding to $\delta = 0$. One test series with pure $BiFeO_3$ samples verified that weight loss was due to reduction of the sample and not vaporization of Bi_2O_3. Recent phase diagrams of the $Bi_2O_3-Fe_2O_3$ system do not imply any intrinsic solid solubility in $BiFeO_3$,[10,11,25] and considerable deviation from a Bi:(Fe + Mn) ratio of 1:1 is not likely. We also confirmed a low solid solubility by preparing a series of $BiFeO_3$ samples with intentional deviation from a Bi:Fe ratio of 1:1. These samples contained the expected secondary phases mullite ($Bi_2Fe_4O_9$) and sillenite ($Bi_{25}FeO_{39}$) and no variation in lattice parameters of $BiFeO_3$ with nominal composition was observed. The nominal Bi/(Fe + Mn) ratio close to unity was inferred for the phase-pure materials.

Characterization. X-ray diffraction (XRD) patterns were collected from 20° 2θ to 96° 2θ with 0.2 mm slits, a step size of 0.014° 2θ, a count time of 3 s per step, and a total acquisition time of 4.5 h per sample with a $\theta-2\theta$ Bruker AXS Focus diffractometer with Cu Kα radiation and a LynxEye position-sensitive detector (PSD). Rietveld refinements were conducted with the software TOPAS R (Bruker AXS), using the space group *R*3*c* (161) in the hexagonal setting. Lattice parameters, lattice strain (Lorentzian profile), and cation positions (setting from Megaw and Darlington[26]) are reported. Oxygen positions did not converge with the present quality of diffraction data.

Differential thermal analysis (DTA) was performed with a Netzsch Model STA 449 C Jupiter system in synthetic air or 5.0 N_2, with a heating and cooling rate of 10 °C/min. Differential scanning calorimetry (DSC) to determine the Néel temperature (T_N) was performed with a Perkin−Elmer Model DSC 7 apparatus with a heating rate of 40 °C/min and powder samples (50−90 mg) contained in aluminum sample pans. Dilatometric traces were recorded in synthetic air with a Netzsch Model DIL 402 C dilatometer, using a heating rate of 2 °C/min. The samples were monolithic ceramic bars with >93% of their crystallographic density. The bars were cooled at a rate of 400 °C/h to avoid cracking when crossing the strongly first-order ferroelectric phase transition.

Four-point electrical conductivity measurements were performed on polycrystalline ceramic samples prepared the same way as those used for dilatometry. Bars polished to a cross-sectional area of 0.2 cm^2 were attached to platinum wires with platinum paint. The four-point method that has been used allows current (I) and voltage (U) to be individually measured (Keithley, Model D500) with two wires passing a current through the sample and two wires a distance of $d = 5$ mm apart measuring the voltage drop across the sample. The conductivity was calculated from $\sigma = Id/UA$, where A is the cross-sectional area normal to the current. Measurements were performed with heating and cooling rates of 3 °C/min in synthetic air. Further details on the experimental setup can be found elsewhere.[27]

Results

Oxygen Stoichiometry. Oxygen hyperstoichiometry (δ) found by thermogravimetrical analysis of $BiFe_{1-x}Mn_xO_{3+\delta}$ samples with different thermal histories is summarized in Table 1. The oxygen stoichiometry is determined by the

(16) (a) Sundaresan, A.; Mangalam, R. V. K.; Iyo, A.; Tanaka, Y.; Rao, C. N. R. *J. Mater. Chem.* **2008**, *18*, 2191. (b) Belik, A. A.; Kolodiazhnyi, T.; Kosuda, K.; Takayama-Muromachi, E. *J. Mater. Chem.* **2009**, *19*, 1593.
(17) Montanari, E.; Calestani, G.; Migliori, A.; Dapiaggi, M.; Bolzoni, F.; Cabassi, R.; Giliolo, E. *Chem. Mater.* **2005**, *17*, 6457.
(18) van Roosmalen, J. A. M.; Cordfunke, E. H. P. *J. Solid State Chem.* **1994**, *110*, 109.
(19) (a) van Roosmalen, J. A. M.; van Vlaanderen, P.; Cordfunke, E. H. P.; Ijdo, W. L.; Ijdo, D. J. W. *J. Solid State Chem.* **1995**, *114*, 516. (b) Töpfer, J.; Goodenough, J. B. *J. Solid State Chem.* **1997**, *130*, 117.
(20) Li, M.; MacManus-Driscoll, J. L. *Appl. Phys. Lett.* **2005**, *87*, 252510.
(21) Yang, C.-H.; Koo, T. Y.; Jeong, Y. H. *Solid State Commun.* **2005**, *134*, 299.
(22) Sahu, J. R.; Rao, C. N. R. *Solid State Sci.* **2007**, *9*, 950.
(23) Kumar, M.; Yadav, K. L. *Appl. Phys. Lett.* **2007**, *91*, 242901.
(24) Azuma, M.; Kanda, H.; Belik, A. A.; Shimakawa, Y.; Takano, M. *J. Magn. Magn. Mater.* **2007**, *310*, 1177.
(25) Maître, A.; François, M.; Gachon, J. C. *J. Phase Equilib.* **2004**, *25*, 59.
(26) Megaw, H. D.; Darlington, C. N. W. *Acta Crystallogr., Sect. A: Found Crystallogr.* **1975**, *31*, 161.
(27) Wærnhus, I.; Vullum, P. E.; Holmestad, R.; Grande, T.; Wiik, K. *Solid State Ionics* **2005**, *176*, 2783.

Table 1. Thermogravimetrical Analysis of $BiFe_{1-x}Mn_xO_{3+\delta}$ with Different Thermal Histories

x	T (°C)	time (h)	atmosphere	history	δ	$x_{Mn(IV)}$	$Mn^{4+}/(Mn)$
0.0	900	0.1	air	quench (q)	0.00 ± 0.01[a]		
0.1	900	0.1	air	quench (q)	0.015 ± 0.005	0.030 ± 0.010	0.30
0.1	825	8.0	air	400 °C/h (c)	0.028 ± 0.005	0.056 ± 0.010	0.56
0.2	900	0.1	air	quench (q)	0.016 ± 0.005	0.031 ± 0.010	0.16
0.2	825	8.0	air	400 °C/h (c)	0.037 ± 0.005	0.074 ± 0.010	0.37
0.3	900	0.1	air	quench (q)	0.030 ± 0.005	0.060 ± 0.010	0.20
0.3	825	8.0	air	400 °C/h (c)	0.059 ± 0.005	0.118 ± 0.010	0.39
0.3	850	0.5	N_2	400 °C/h (c)	0.00[b]	0[b]	0[b]

[a] Data taken from ref 20. [b] Assuming negligible amounts of Mn^{4+} after annealing in N_2.

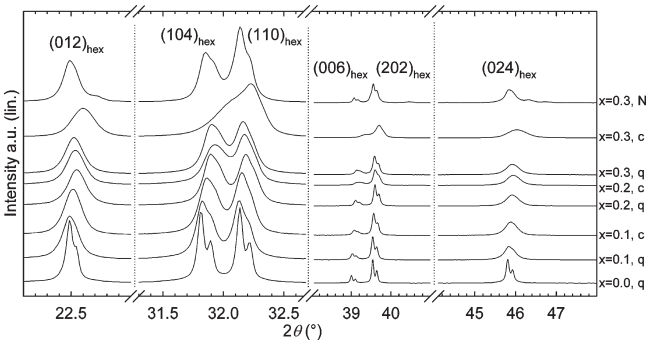

Figure 1. X-ray diffractograms displaying selected Bragg peaks reflecting the influence of Mn substitution (x in $BiFe_{1-x}Mn_xO_{3+\delta}$) and thermal history on the crystal structure. Patterns labeled "q" denote materials quenched in air, patterns labeled "c" denote materials cooled at a rate of 400 °C/h in air, and the pattern labeled "N" represents material annealed in a flowing N_2 atmosphere (see Table 1).

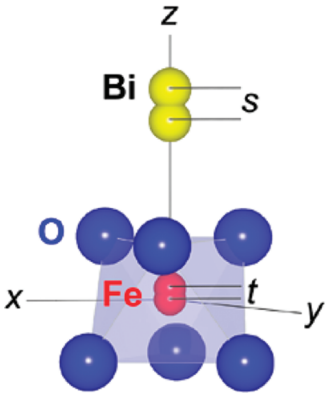

Figure 2. Part of the crystal structure of $BiFeO_3$ in the hexagonal setting. The displacements s(Bi) and t(Fe/Mn) distinguish the polar space group $R3c$ from the centrosymmetric space group $R\bar{3}c$. Antiferrodistortive rotation (not shown) of the $FeO_{6/2}$ octahedra about the hexagonal z-axis distinguishes $R3c$ from the space group $R3m$.

thermal history of the materials, which is due to the possible variation of the valence state of Mn (Mn^{3+} and Mn^{4+}). Samples annealed in N_2 were assumed to be stoichiometric, with respect to oxygen. Two significant trends are found: (1) air-quenched samples display less excess oxygen than air-cooled samples with equal Mn substitution, and (2) oxygen hyperstoichiometry increases as the manganese content increases under equal thermal history. More reducing conditions at higher temperatures yields less excess oxygen, in accordance with the predominance diagram of the Mn−O binary system.[28]

Crystal Structure. Room-temperature XRD patterns for all samples could be indexed with the space group $R3c$; thus, the ground-state space group does not change within the range of Mn substitution and oxygen hyperstoichiometry investigated here. Selected Bragg reflections from XRD shown in Figure 1 illustrate the effect of Mn substitution (x) and oxygen hyperstoichiometry (δ). The observed splitting of the pesudo-cubic (110) reflection into $(104)_{hex}$ and $(110)_{hex}$ reflections is due to the rhombohedral distortion of the unit cell. This splitting, and the analogous decrease of the splitting of the (111) pseudo-cubic reflection into $(006)_{hex}$ and $(202)_{hex}$ reflections, with increasing manganese content (x) and excess oxygen (δ) reveal that the unit cell becomes less distorted.

A portion of the $BiFeO_3$ crystal structure with space group $R3c$ in the hexagonal setting is displayed in Figure 2. Compared to the ideal, cubic structure with space group $Pm\bar{3}m$, cooperative displacements of Bi^{3+} by s and Fe^{3+} by t along the [111] pseudo-cubic axis (|| [001] hexagonal axis) alone gives the polar space group $R3m$. Antiferrodistortive rotation of the oxygen octahedra about the pseudo-cubic [111] axis alone results in the centrosymmetric space group $R\bar{3}c$. Combining these two symmetry-lowering distortions yields the space group $R3c$.[26]

Normalized lattice parameters $a = 2^{-1/2}a_{hex}$, $c = (12)^{-1/2}c_{hex}$ and primitive unit cell volume obtained by Rietveld refinement of the XRD patterns as a function of Mn substitution, is reported in Figure 3a. The lattice parameter c, parallel to the spontaneous polarization, decreases more rapidly with Mn substitution than the lattice parameter a, implying that the unit cell becomes less distorted, which is consistent with the evolution of the splitting of the $(110)_{cub}$ reflection in Figure 1. Air-cooled samples with enhanced excess oxygen (open symbols in Figure 3a; also see Table 1) display substantially smaller lattice parameters and unit-cell volume than the quenched samples (gray-filled symbols). Filled symbols represent oxygen stoichiometric material with $x = 0.3$ annealed in N_2. Lattice parameters and unit-cell volume also each decrease with increasing Mn substitution for oxygen stoichiometric materials.

Polar cation displacements (see Figure 3b) confirm that both Mn substitution and excess oxygen gives a less-distorted crystal structure. The displacement of Bi on the A site is more sensitive to Mn substitution and excess oxygen than the displacement of Fe and Mn on the B site, where the substitution occurs. The quantity $s - t$ is the

(28) Fritsch, S.; Navrotsky, A. *J. Am. Ceram. Soc.* **1996**, *79*, 1761.

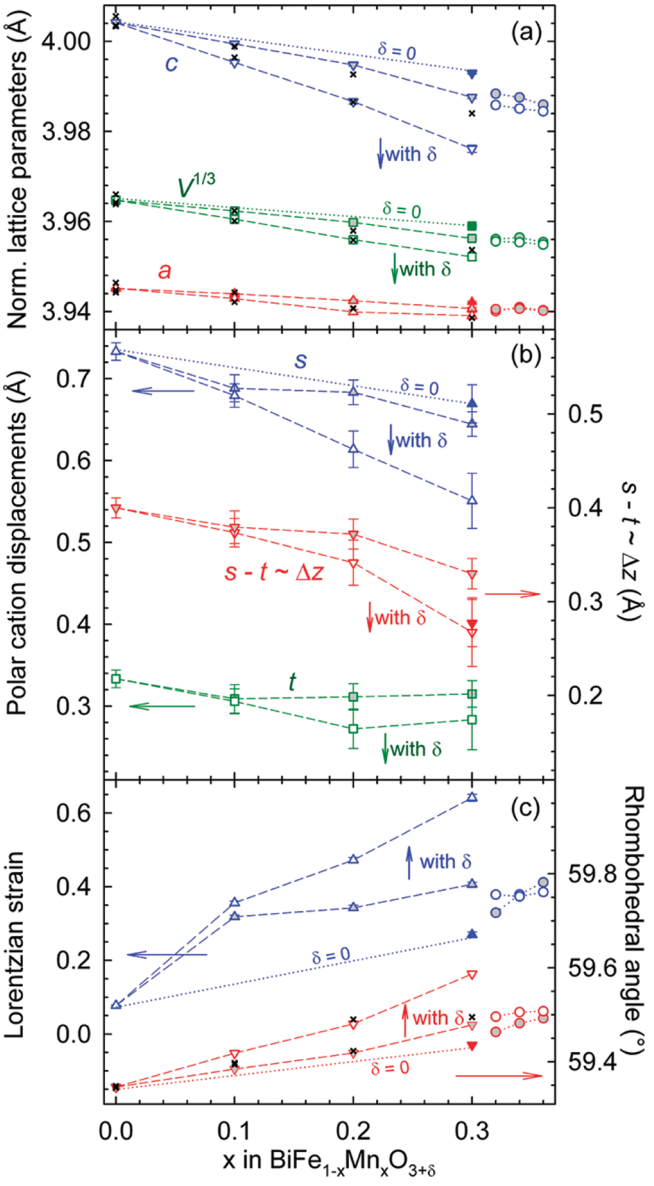

Figure 3. Crystallographic properties obtained from Rietveld refinement of XRD patterns in Figure 1. Gray-filled symbols denote quenched samples, open symbols represent samples cooled at a rate of 400 °C/h, and filled symbols denote the $x=0.3$ sample fired in N_2. Circles refer to the samples whose data are presented in Figure 8 (shown later in this paper), where the gray-filled and open symbols correspond to samples fired at 900 and 800 °C, respectively: (a) normalized lattice parameters ($a=2^{-1/2}a_{hex}$ and $c=(12)^{-1/2}c_{hex}$) and primitive unit-cell volume; (b) polar cation displacements s(Bi) and t(Fe/Mn) and cooperative polar displacements ($s-t$; see explanation in text); and (c) refined Lorentzian strain and rhombohedral angle of the unit cell in rhombohedral setting (60° correspond to the ideal cubic aristotype structure). Literature values have been taken from refs 22 and 30 and are denoted as **x**.

relative displacement of Bi and Fe/Mn or, equivalently, the displacement of Fe/Mn from its centrosymmetric position with the unit cell fixed with Bi *in origo*.[29] Oxygen positions, which are linked to the antiferrodistortive rotation of oxygen octahedra about the $[001]_{hex}$ axis, did not converge during the refinements and are not reported; thus, neutron diffraction data are required for a detailed study of the influence of Mn substitution and

(29) Selbach, S. M.; Tybell, T.; Einarsrud, M.-A.; Grande, T. *Chem. Mater.* **2007**, *19*, 6478.

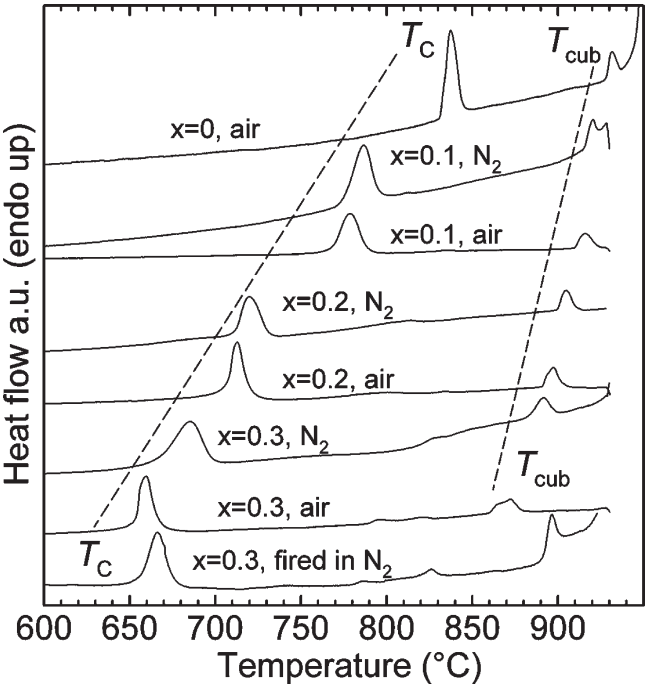

Figure 4. Differential thermal analysis (DTA) traces identifying the transitions to the paraelectric phase (T_C) and the paraelastic, cubic phase (T_{cub}). Labels refer to x in $BiFe_{1-x}Mn_xO_{3+\delta}$ and the atmosphere used during the measurements. Quenched samples and the $x=0.3$ sample fired in N_2 were measured in a flowing N_2 atmosphere; cooled samples were measured in synthetic air.

excess oxygen on this structural feature. Oxygen positions obtained from neutron data reported by Sosnowska et al. show that the antiferrodistortive rotation of the oxygen octahedra decreases with increasing Mn substitution.[30]

The rhombohedral angle α_{rh} (Figure 3c) increases as the Mn substitution increases and δ increases from the value of 59.35° in pure $BiFeO_3$. A rhombohedral angle of 60° corresponds to the ideal cubic perovskite structure, and it is related to the normalized lattice parameters by[26] $\alpha_{rh}=2\arcsin(3a/2\sqrt{3a^2+6c^2})$.

The refined Lorentzian strain increases as the Mn substitution and oxygen excess each increase, in concordance with the systematic broadening of the Bragg reflections in Figure 1. The full width at half maximum (FWHM) of the Bragg reflections increases with both increasing x and δ. The FWHM value is substantially larger for "sample 0.3, c" than "sample 0.3, N" (see caption of Figure 1). The influence of excess oxygen, which has not been taken into consideration in previous reports on Mn-substituted $BiFeO_3$, is the likely origin of the spread in literature values from refs 22 and 30, denoted by **x** in Figure 3.

Phase Transitions. First-order structural transitions are readily detected by differential thermal analysis, as shown in Figure 4. Quenched samples with less excess oxygen were measured in a N_2 atmosphere, whereas air-cooled samples with more excess oxygen were measured in synthetic air to retain the difference in oxygen stoichiometry during the measurements. The ferroelectric Curie temperature (T_C) is substantially reduced by substituting with Mn, in agreement with previous reports.[22] From the

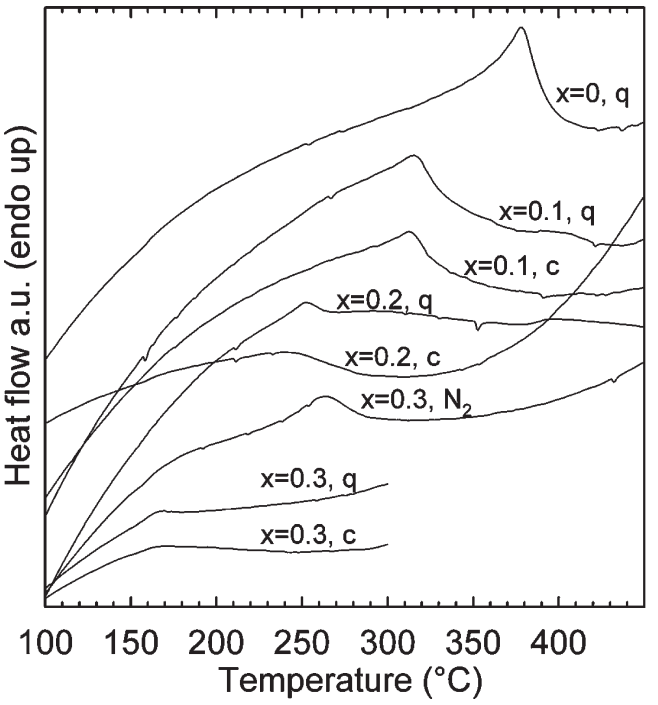

Figure 5. Differential scanning calorimetry (DSC) traces identifying the Néel temperature (T_N) of $BiFe_{1-x}Mn_xO_{3+\delta}$. Labels refer to the thermal history of the samples and are explained in Table 1.

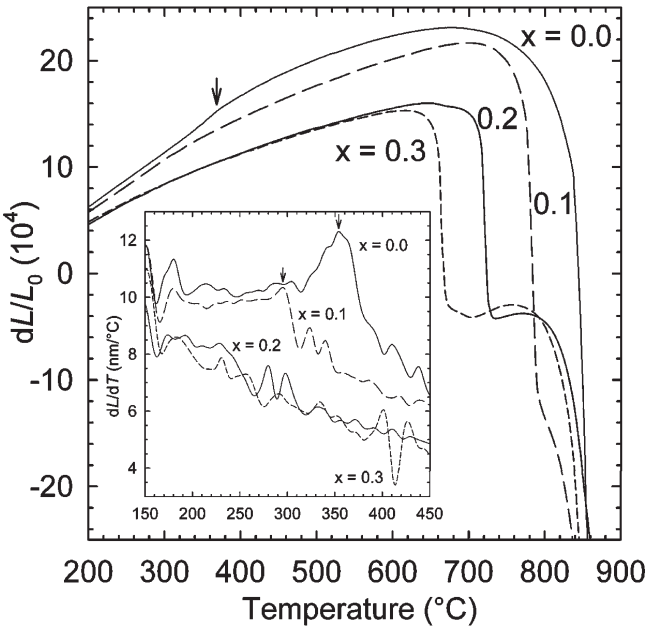

Figure 6. Dilatometric traces measured in synthetic air on polycrystalline bars; labels correspond to x in $BiFe_{1-x}Mn_xO_{3+\delta}$. The arrow denotes the continuous expansion anomaly associated with the Néel transition at T_N. Inset: differential thermal expansion around T_N.

three $x = 0.3$ samples, it is also evident that δ affects T_C, which is discussed further below. The paraelectric structure of both pure $BiFeO_3$ and $BiFe_{0.7}Mn_{0.3}O_{3+\delta}$ has recently been shown to be orthorhombic *Pbnm*,[13,14] which is ferroelastic.[10] The transition from paraelectric, ferroelastic *Pbnm* to ideal cubic, paraelastic $Pm\bar{3}m$ is labeled T_{cub}. Mn substitution increases the temperature interval of the *Pbnm* polymorph, and it also stabilizes the $Pm\bar{3}m$ polymorph at lower temperatures. The dashed lines show that T_{cub} is less influenced by Mn substitution than T_C. Oxygen hyperstoichiometry reduces the value of T_{cub}, compared to oxygen stoichiometric Mn-substituted materials.

Differential scanning calorimetry (DSC) traces reveal the T_N value as an endothermal peak (see Figure 5). The T_N value decreases substantially with both x and δ, compared to the pure $BiFeO_3$ sample with $T_N = 370$ °C. The endothermal peaks become less sharp with increasing x and δ, suggesting that the transition becomes smeared out over a larger temperature interval, possibly reflecting structural disorder. It was not possible to identify, with certainty, the T_N value in $BiFe_{0.7}Mn_{0.3}O_{3.06}$ and materials with $x > 0.3$ by DSC.

Dilatometric traces in Figure 6 recorded on polycrystalline bars confirm the phase-transition temperatures found by calorimetry. Across the ferroelectric transition at T_C, the volume of transition ($\Delta_{trs}V$) is large and negative for all x but decreases as x increases. The effects of sintering and creep are superimposed on the crystallographic expansion, thus absolute values for $\Delta_{trs}V$ at T_C could not be extracted. We have previously shown that $\Delta_{trs}V$ at T_{cub} is positive, but significantly smaller than $\Delta_{trs}V$ at T_C.[14] Thermal expansion anomalies across the antiferromagnetic transition at T_N are envisaged by the differential traces in the inset of Figure 6.

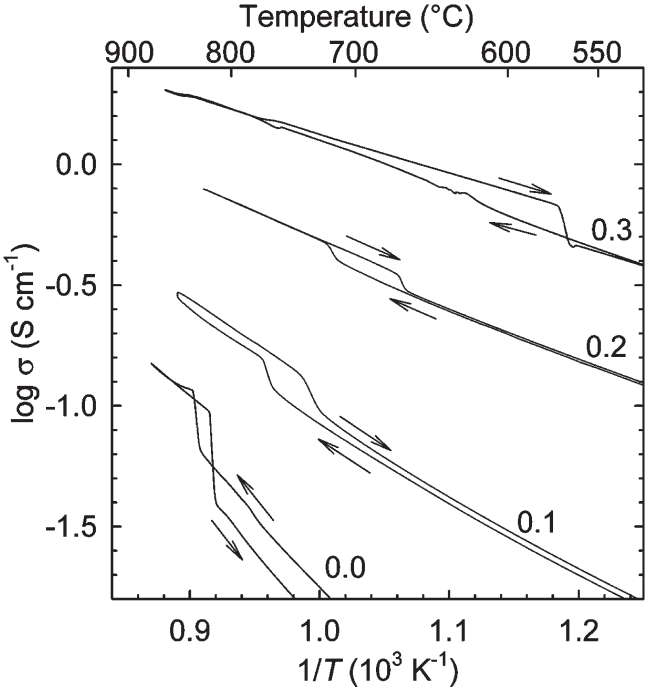

Figure 7. Electrical conductivity traces measured in synthetic air on polycrystalline bars. Arrows depict traces upon heating and cooling.

Electrical Conductivity. The electrical conductivity, measured in synthetic air, is displayed in Figure 7, showing that $BiFe_{1-x}Mn_xO_{3+\delta}$ displays semiconductivity for all temperatures, x values, and δ values that were investigated.

(30) Sosnowska, I.; Schäfer, W.; Kockelmann, W.; Andersen, K. H.; Troyanchuk, I. O. *Appl. Phys. A: Mater. Sci. Process.* **2002**, *74*, S1040.

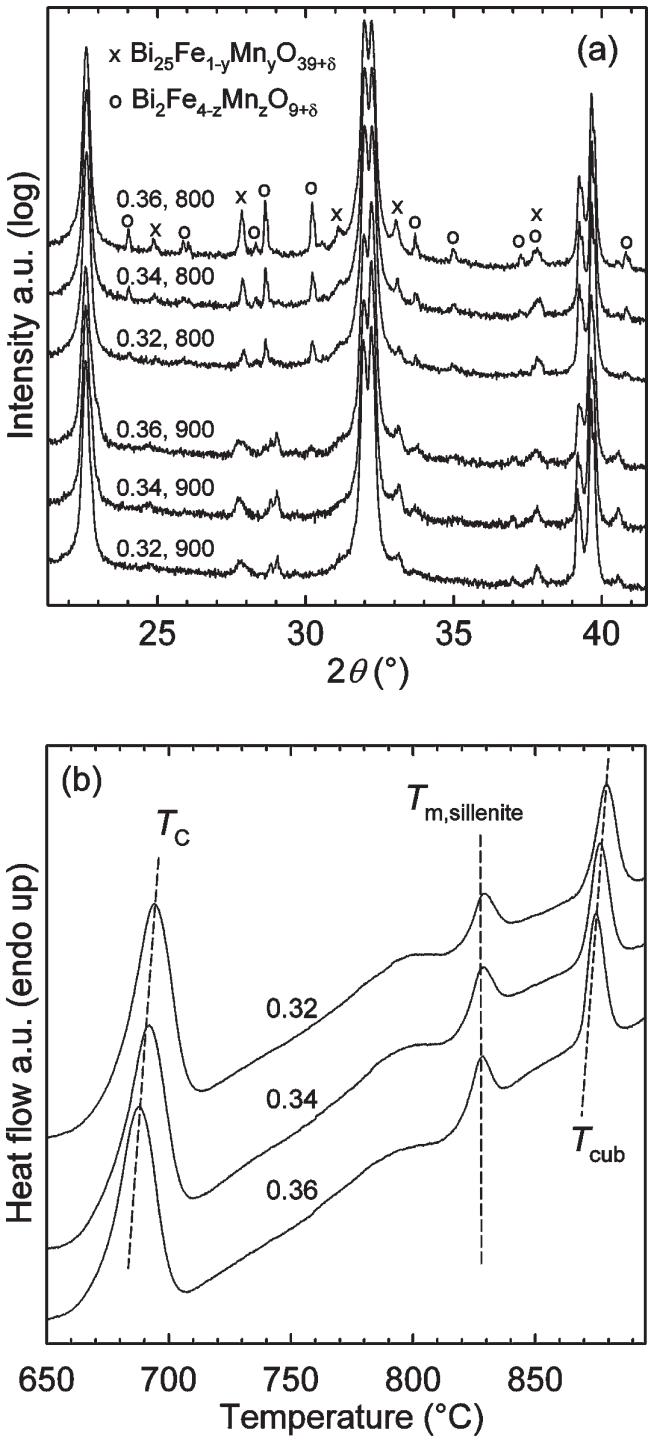

Figure 8. (a) XRD patterns of samples with compositions beyond the ambient pressure solid solubility limit. Labels refer to x in $BiFe_{1-x}Mn_xO_{3+\delta}$ and the firing temperature. (b) DTA traces for samples fired at 900 °C, measured in flowing N_2 atmosphere.

The conductivity increases with Mn substitution, while the log σ vs $1/T$ slope decreases, indicating a lower activation energy of conduction. The conductivity anomaly that is due to the ferroelectric phase transition has been related to the large volume contraction going from the ferroelectric to the paraelectric polymorph.[12,14] The transition temperatures are in good accordance with the DTA and dilatometry traces in Figures 4 and 6. With increasing x and decreasing T_C, the discontinuity in conductivity that is associated with T_C becomes smaller. This feature can be rationalized from the smaller volume of transition with increasing x, as demonstrated in Figure 6.

Thermal hysteresis of the conductivity traces, associated with the first-order nature of the ferroelectric transition, increases with Mn substitution, thus the paraelectric structure becomes metastable to lower temperatures upon cooling, compared to the transition temperature upon heating. Increasing thermal hysteresis about T_C with increasing substitution level is opposite of the behavior reported for the ferroelectric model system $PbZr_{1-x}Ti_xO_3$ (PZT).[31] In PZT, both Zr and Ti have stable oxidation states of 4+, while Mn is found as 3+ and 4+ in $BiFe_{1-x}Mn_xO_{3+\delta}$, depending on the oxygen stoichiometry. This additional chemical degree of freedom in the $BiFe_{1-x}Mn_xO_{3+\delta}$ system allows two solids to coexist with a gas phase, which is consistent with Gibbs phase rule, explaining the increasing thermal hysteresis with increasing x in $BiFe_{1-x}Mn_xO_{3+\delta}$. The influence of atmosphere and oxygen stoichiometry on the electrical conductivity at high temperatures has been reported in detail for $x = 0.3$ elsewhere.[14]

Solubility. A series of three samples with compositions $x = 0.32$, 0.34, and 0.36 was characterized to elucidate the solid solubility limit of Mn in $BiFe_{1-x}Mn_xO_{3+\delta}$ at ambient pressure. The ambient pressure solid solubility limit is usually reported as being close to $x = 0.3$, whereas high-pressure synthesis enables complete solid solution.[21,24] In Figure 8a, XRD patterns are displayed on a logarithmic scale to highlight any secondary phases found in these samples. All reflections due to secondary phases could be indexed according to the patterns of $Bi_{25}Fe_{1-y}Mn_yO_{39+\delta}$ (sillenite, $Bi_{25}FeO_{39}$, JCPDF File Card No. 46-0416) and $Bi_2Fe_{4-z}Mn_zO_{9+\delta}$ (mullite, $Bi_2Fe_4O_9$, JCPDF File Card No. 72-1832). Materials fired at 900 °C clearly contain less secondary phases than the samples fired at 800 °C. This suggests that the solubility of Mn increases with increasing temperature. If exceeding the solid solubility limit simply led to manganese going into the secondary phases sillenite and mullite, one would expect the structural phase-transition temperatures of the perovskite phase to be equal for the three compositions with $x > 0.3$. However, as shown in Figure 8b, both T_C and T_{cub} for the materials fired at 900 °C decrease as x increases, while the melting temperature of the sillenite secondary phase does not change, implying that the solid solubility limit at ambient pressure is higher than 0.3, in agreement with the systematic decrease in lattice parameter c for $x > 0.3$ (see Figure 3a).

Discussion

Defect Chemistry. Oxygen deficiency is well-known in perovskite materials, while oxygen hyperstoichiometry is far less common. Excess oxygen cannot be accommodated as interstitial ions in perovskites because the crystal

(31) Rossetti, G. A., Jr.; Navrotsky, A. *J. Solid State Chem.* **1999**, *144*, 188.

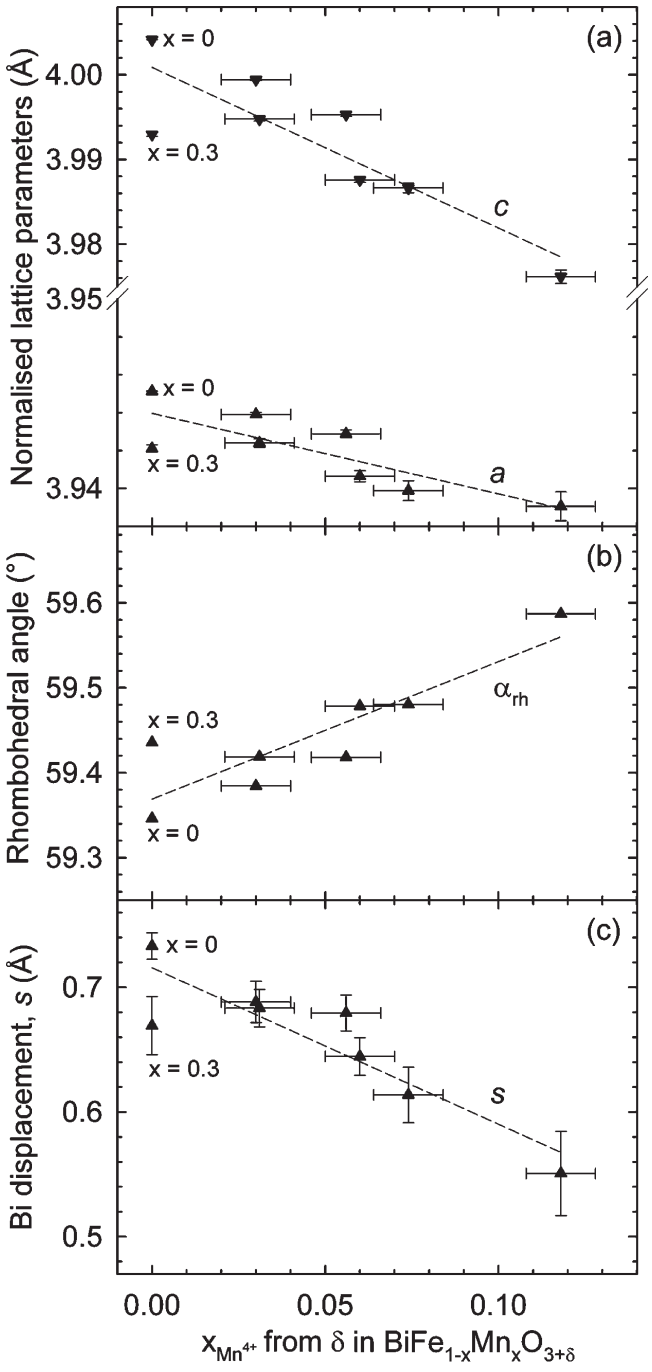

Figure 9. (a) Normalized lattice parameters, as a function of Mn^{4+} content derived from δ. (b) Rhombohedral angle, as a function of Mn^{4+}. (c) Polar displacement of Bi (s), as a function of Mn^{4+}. Dashed lines are present as guides to the eye.

structure is too close-packed.[18] To retain charge equilibrium, excess oxygen is compensated by cation vacancies. The addition of excess oxygen to $BiFe_{1-x}Mn_xO_3$ can be described by the Kröger−Vink point-defect equilibrium:

$$\frac{\delta}{2}O_2 \rightleftarrows \delta O_O^{\times} + 2\delta h^{\bullet} + \frac{\delta}{3}V_{Bi}''' + \frac{\delta}{3}V_{Fe,Mn}''' \qquad (1)$$

Cation vacancies in the Bi and Fe/Mn sublattices are denoted as V_{Bi}''' and $V_{Fe,Mn}'''$, respectively. Holes ($h^{\bullet}$) appear when Mn^{3+} is oxidized to Mn^{4+}: $Mn^{4+} \rightleftarrows Mn^{3+} + h^{\bullet}$. The Mn^{4+}:δ ratio is 2:1, and the fraction of Mn ions present as Mn^{4+} is $2\delta/x$. Unsubstituted $BiFeO_{3+\delta}$ is stoichiometric within $\delta < 0.01$,[20] and iron has been shown to exist in the 3+ oxidation state.[32] Thus, oxygen hyperstoichiometry is predominantly charge-compensated by oxidation of Mn^{3+} to Mn^{4+} in $BiFe_{1-x}Mn_xO_{3+\delta}$.[14] Therefore, a more correct formula for oxygen hyperstoichiometric Mn-substituted $BiFeO_3$ is $Bi_{1-\delta/3}(Fe_{1-x}Mn_x)_{1-\delta/3}O_3$. Excess oxygen compensated by cation vacancies and mixed Mn valence of 3+/4+ have also been reported for the related systems $BiMnO_{3+\delta}$, $LaMnO_{3+\delta}$, and $La_{0.5}Bi_{0.5}Mn_{0.5}Fe_{0.5}O_{3.09}$.[16,19,33] A larger concentration of vacancies at the A site than the B site, $Bi_{1-y}(Fe_{1-x}Mn_x)_{1-z}O_3$, with $y > z$, is known to occur in $La_{1-y}Mn_{1-z}O_3$.[34] The samples studied in the present investigation would not reveal if significant cation nonstoichiometry is possible in Mn-substituted $BiFeO_3$.

Crystal Structure. Decreasing unit-cell volume (Figure 3a) with increasing x and δ is consistent with the decreasing polar displacement of Bi^{3+}, s (see Figure 3b). The lattice parameter c is parallel to the polar cation displacements, and it is also the most sensitive to x and δ. However, the lattice parameter a, normal to the polarization, also decreases with x and δ. Both c and a are smaller for oxygen stoichiometric $BiFe_{0.7}Mn_{0.3}O_3$ than for pure $BiFeO_3$. Substantially smaller unit-cell volumes with increasing excess oxygen result naturally from the smaller ionic radii[35] of Mn^{4+} than Mn^{3+} and Fe^{3+}. Chemical expansion is well-established in perovskites with oxygen nonstoichiometry compensated by multiple cation valences.[36] The influence of the oxidation state of manganese is demonstrated in Figure 9, where the lattice parameters, rhombohedral angle, and Bi displacement are all shown to correlate well with the fraction of Mn^{4+} inferred from δ. Given that the antiferrodistortive rotation of oxygen octahedra decreases with x,[30] one would expect the lattice parameter a to increase with x, because the Shannon radii of Fe^{3+} and Mn^{3+} are equal. Decreasing the antiferrodistortive rotation of oxygen octahedra alone should increase the lattice parameter;[37] thus, Mn^{3+} seems to possess a smaller ionic radius than Fe^{3+} in $BiFe_{1-x}Mn_xO_{3+\delta}$. Decreasing the unit-cell volume with increasing δ is also known from $LaMnO_{3+\delta}$.[38]

The combination of decreasing unit-cell distortion and increasing Lorentzian strain (see Figure 3c) implies that

(32) Kothari, D.; Raghavendra Reddy, V.; Gupta, A.; Phase, D. M.; Lakshmi, N.; Deshpande, S. K.; Awasthi, A. M. *J. Phys.: Condens. Matter* **2007**, *19*, 136202.
(33) Kundu, A. K.; Ranjith, R.; Kundys, B.; Nguyen, N.; Caignaert, V.; Pralong, V.; Prellier, W.; Raveau, B. *Appl. Phys. Lett.* **2008**, *93*, 052906.
(34) (a) Töpfer, J.; Goodenough, J. B. *Solid State Ionics* **1997**, *101−103*, 1215. (b) De Silva, P. S. I. P. N.; Richards, F. M.; Cohen, L. F.; Alonso, J. A.; Martínez-Lope, M. J.; Casais, M. T.; Thomas, K. A.; MacManus-Driscoll, J. L. *J. Appl. Phys.* **1998**, *83*, 394.
(35) Shannon, R. D. *Acta Crystallogr., Sect. A: Found Crystallogr.* **1976**, *32*, 751.
(36) (a) Adler, S. B. *J. Am. Ceram. Soc.* **2001**, *84*, 2117. (b) Chen, X.; Yu, J.; Adler, S. B. *Chem. Mater.* **2005**, *17*, 4537.
(37) Megaw, H. D. *Mater. Res. Bull.* **1971**, *6*, 1007.
(38) (a) Zhou, X.-D.; Pederson, L. R.; Cai, Q.; Yang, J.; Scarfino, B. J.; Kim, M.; Yelon, W. B.; James, W. J.; Anderson, H. U.; Wang, C. *J. Appl. Phys.* **2006**, *99*, 08M918. (b) Huang, Q.; Santoro, A.; Lynn, J. W.; Erwin, R. W.; Borchers, J. A.; Peng, J. L.; Peng, R. L.; Greene, R. L. *Phys. Rev. B* **1997**, *44*, 14987.

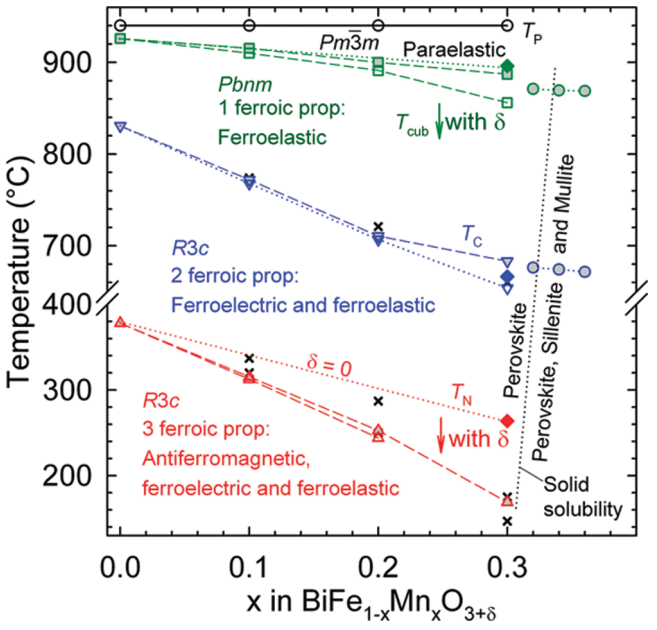

Figure 10. Phase diagram of the pseudo-binary system $BiFeO_3-BiMnO_{3+\delta}$ at ambient pressure, showing the stability regions of three, two, one, and zero ferroic properties, as a function of Mn substitution (x) and the influence of oxygen hyperstoichiometry (δ). T_N, T_C, T_{cub}, and T_P denote the antiferromagnetic Néel, ferroelectric Curie, transition to cubic, and peritectic decomposition temperatures, respectively. Filled symbols are for the $x=0.3$ sample annealed in N_2, gray-filled symbols for samples for quenched samples and open symbols for samples cooled at a rate of 400 °C/h. The dotted, almost vertical, line is an estimate for the ambient pressure solid solubility limit of Mn. Circles are critical temperatures based on DTA traces in Figure 8b. Literature values adopted from refs 21, 22, and 30 are denoted as **x**.

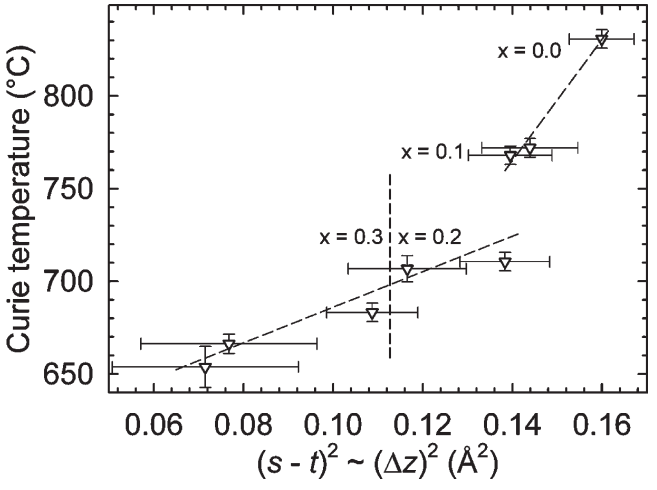

Figure 11. The ferroelectric Curie temperature plotted against the square of polar cation displacements, according to the relation reported by Abrahams et al.[46] There are two apparent linear regions, with a crossover between $x=0.1$ and $x=0.2$.

lattice strain and/or structural disorder is introduced by both Mn substitution and excess oxygen. The oxygen stoichiometric $x = 0.3$ sample (filled symbol, Figure 3c) shows that Mn substitution causes some lattice strain, even for oxygen stoichiometric samples. Comparison of the three different oxygen stoichiometries for $x = 0.3$, relative to the influence of manganese content, indicates that excess oxygen causes larger lattice strain than the introduction of Mn alone. Inhomogenous oxygen

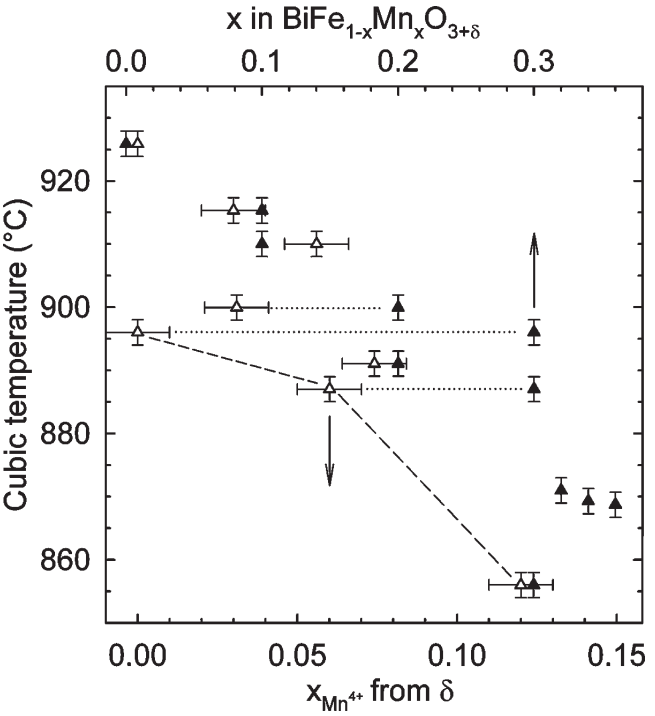

Figure 12. The temperature of transition to the ideal, cubic aristotype structure as a function of x (filled symbols, upper x-axis) and as a function of content of oxidized Mn^{4+} due to oxygen hyperstoichiometry δ (open symbols, lower x-axis). The two horizontal dotted lines connect the same data points plotted on the two different x-axes. The dashed line highlight the influence of the content on Mn^{4+} for three different materials with 30% Mn and different oxygen stoichiometry.

stoichiometry throughout the sample, and associated gradients in the concentration of Mn^{4+}, is also anticipated, because cation diffusion is slow in perovskites.[39] The apparent discontinuity in lattice parameters between the series of quenched samples with $x \leq 0.3$ (gray-filled symbols, Figure 3b) and the series with $x > 0.3$ is probably due to the sensitivity of the crystal structure to the thermal history, because these samples were fired in separate series (possibly with different quench rates).

The polar displacement of the A cation Bi^{3+} is far more sensitive to x than the displacement of the B cations, although substitution occurs on the B-site. These displacements are coupled, and the electrostatic energy strongly favors unidirectional displacement along the polar axis.[40] The substantial decrease in displacement of Bi may thus reflect disorder introduced on the B-site with Mn, because Mn^{3+} is a high spin (HS) d^4 Jahn–Teller active cation opposed to HS d^5 Fe^{3+}. Excess oxygen also contributes to B-site disorder, as it is compensated by both vacancies and d^3 Mn^{4+}, resulting in four different occupants of the B site; Fe^{3+}, Mn^{3+}, Mn^{4+}, and a vacancy. B-site disorder is a likely origin of the increasing broadening of the Bragg reflections with increasing x and δ in Figure 1, and the increasing Lorentzian strain in Figure 3c.

Phase Diagram. The phase diagram shown in Figure 10 is the main conclusion from this work. It demonstrates

(39) Palcut, M.; Wiik, K.; Grande, T. *J. Phys. Chem. C* **2007**, *111*, 813.
(40) Thomas, N. W.; Beitollah, A. *Acta Crystallogr., Sect. B: Struct. Sci.* **1994**, *50*, 549.

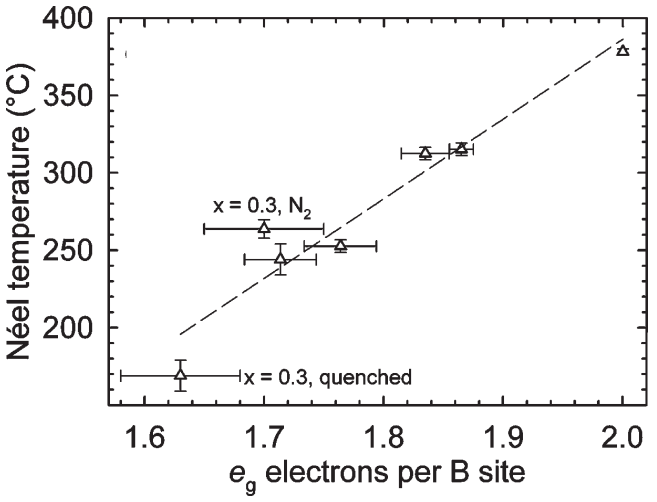

Figure 13. Graph of the Néel temperature, which displays a correlation with the number of e_g electrons on the B-site.

the stability range of regions with three, two, one, or zero ferroic orders, in terms of temperature, manganese content, and excess oxygen. Each of the transitions associated with the onset of a ferroic order are discussed below.

Ferroelectric Transition. Ferroelectricity is a cooperative phenomenon, and chemical substitution, defects, and finite size effects are known to influence both the spontaneous polarization and Curie temperature of ferroelectric materials.[41] In perovskites with B cations with nonzero number of *d*-electrons, ferroelectricity can occur due to partial covalent bonding between O 2*p* orbitals and a $6s^2$ lone pair on the A cation.[42] Even though the $6s^2$ lone pair of Bi^{3+} is considered the primary driving force for ferroelectricity,[42,43] the substantial decrease in T_C of 5−6 °C per % Mn substituted demonstrates the importance of the B site. Six-coordinated HS Fe^{3+} and HS Mn^{3+} are equal in size, according to their Shannon radii (0.645 Å), although it appears that Mn^{3+} occupies a smaller volume than Fe^{3+}, as previously mentioned. The main difference between HS Fe^{3+} and Mn^{3+} is the number of e_g electrons (2 and 1, respectively). The e_g orbitals of Mn^{3+} possess higher energy than those of Fe^{3+}, because of smaller effective nuclear charge. Thus, partial covalent bonding between Fe 3*d* and O 2*p* orbitals may be more important to ferroelectricity in $BiFeO_3$ than usually recognized. Partial covalent bonding between Ti 3*d* and O 2*p* orbitals stabilizes the ferroelectric phase in $BaTiO_3$ and $PbTiO_3$,[44] and partial covalency was also found between Fe 3*d* and O 2*p* orbitals in a theoretical study of $BiFeO_3$ by Ravindran et al.[43] The observed structural disorder and loss of structural coherence caused by Mn substitution, as evidenced by the increasing FWHM of the Bragg reflections (see Figure 1) and lattice strain (see Figure 3c), may thus destabilize the ferroelectric phase. Site disorder is detrimental to a cooperative phenomenon as ferroelectricity. Based on this, B-site disorder is proposed to be important for both the decreasing polar displacements of Bi and the observed decrease of T_C. In analogy, the substitution of Sc for Mn in $BiMnO_3$ has been reported to disrupt the short-range order of the crystal lattice.[45] This substitution also affected the long-range order of the structure where correlations between Mn^{3+} and Bi^{3+} are important, and not only the ordering of the Bi^{3+} $6s^2$ lone pairs. Systematic studies of the effects of substitution thus may shed light on the origins of multiferroic behavior in $BiFeO_3$ and $BiMnO_3$, and their solid solutions.

Abrahams et al. reported a simple, empirical relation between Curie temperature and polar cation displacements Δz relative to a centrosymmetric reference structure; $T_C = (\kappa/2k_B)(\Delta z)^2$, where κ is a force constant and k_B the Boltzmann's constant.[46] For the polar space group *R*3*c*, the quantity Δz in the Abrahams et al. relation corresponds to $s - t$, where the unit cell is anchored by $z_A = 0$.[29] A plot of T_C vs $(s - t)^2 \approx (\Delta z)^2$ indicates two regions of linearity with a crossover between $x = 0.1$ and 0.2, as shown in Figure 11. The ferroelectric polymorph is destabilized by Mn substitution, with respect to temperature, and according to the proposed $P-T$ phase diagram,[47] one would expect that Mn substitution also destabilizes the *R*3*c* phase with respect to pressure. High-pressure studies of $BiFe_{1-x}Mn_xO_{3+\delta}$ could improve the understanding of the high-pressure[48] behavior of pure $BiFeO_3$, in analogy with our recent report on $x = 0.3$ at high temperatures.[14]

Transition to Cubic Structure. The cubic, paraelastic phase is stabilized at lower temperatures with increasing Mn and δ, as evidenced by the DTA traces in Figure 4. The cubic temperature is plotted as a function of both x and fraction of Mn^{4+} in Figure 12. Horizontal dotted lines connect T_{cub} of the same materials, plotted on two different x-axes. The cubic phase is stabilized by Mn substitution, also for oxygen stoichiometric samples with negligible amounts of Mn^{4+}. The dashed line connecting three samples with $x = 0.3$ envisage the stabilization of the cubic phase by increasing Mn^{4+} content, which is due to excess oxygen. Under ambient conditions, perovskites only adopt the cubic structure when the Goldschmidt tolerance factor,[49] $t = 2^{-1/2}(r_A + r_O)/(r_B + r_O)$ (where r_A,

(41) Lines, M. E.; Glass, A. M. *Principles and Applications of Ferroelectrics and Related Materials*; Oxford University Press: Oxford, U.K., 2004.
(42) (a) Hill, N. A. *J. Phys. Chem. B* **2000**, *104*, 6694. (b) Neaton, J. B.; Ederer, C.; Waghmare, U. V.; Spaldin, N. A.; Rabe, K. M. *Phys. Rev. B* **2005**, *71*, 014113.
(43) Ravindran, P.; Vidya, R.; Kjekshus, A.; Fjellvåg, H.; Eriksson, O. *Phys. Rev. B* **2006**, *74*, 224412.
(44) Cohen, R. E. *Nature* **1992**, *358*, 136.
(45) Yokosawa, T.; Belik, A. A.; Asaka, T.; Kimoto, K.; Takayama-Muromachi, E.; Matsui, Y. *Phys. Rev. B* **2008**, *77*, 024111.
(46) Abrahams, S. C.; Kurtz, S. K.; Jameson, P. B. *Phys. Rev.* **1968**, *172*, 551.
(47) Catalan, G.; Scott, J. F. *Adv. Mater.* **2009**, *21*, 2463.
(48) (a) Gavriliuk, A. G.; Struzhkin, V. V.; Lyubutin, I. S.; Ovchinnikov, S. G.; Hu, M. Y.; Chow, P. *Phys. Rev. B* **2008**, *77*, 155112. (b) Haumont, R.; Bouvier, P.; Pashkin, A.; Rabia, K.; Frank, S.; Dkhil, B.; Crichton, W. A.; Kuntscher, C. A.; Kreisel, J. *Phys. Rev. B* **2009**, *79*, 184110.(c) Redfern, S. A. T.; Walsh, J. N.; Clark, S. M.; Catalan, G.; Scott, J. F. Paper No. condmat arXiv: 0901.3748. http://arxiv.org/pdf/0901.3748.(d) Belik, A. A.; Yusa, H.; Hirao, N.; Ohishi, Y.; Takayama-Muromachi, E. *Chem. Mater.* **2009**, *21*, 3400.
(49) Goldschmidt, V. M. *Naturwissenschaften* **1926**, *14*, 477.

r_B and r_O are the ionic radii), is close to unity. Oxygen stoichiometric $BiFe_{0.7}Mn_{0.3}O_3$ displays a T_{cub} value that is 30−35 °C lower than that for pure $BiFeO_3$, which is consistent with a higher tolerance factor for $x = 0.3$ than $x = 0$, as Mn^{3+} is apparently smaller than Fe^{3+} in $BiFe_{1-x}Mn_xO_{3+\delta}$. Oxygen hyperstoichiometry is charge-compensated by oxidation of Mn^{3+} to Mn^{4+}, according to eq 1. While octahedrally coordinated HS Mn^{3+} is $t_{2g}^3e_g^1$, Mn^{4+} is $t_{2g}^3e_g^0$, and thus substantially smaller (0.530 Å). Excess oxygen thus causes an increase in the effective tolerance factor of the system, accounting for the stabilization of the cubic phase to lower temperatures with increasing δ. Similarly, the polyhedral volume ratio V_A/V_B increases toward 5.0 with increasing δ, which is the value in the absence of octahedral tilting.[40,50]

Antiferromagnetic Transition. The B cations present in $BiFe_{1-x}Mn_xO_{3+\delta}$ in this study are Fe^{3+} (d^5 HS), Mn^{3+} (d^4 HS), and Mn^{4+} (d^3); thus, the number of e_g electrons are 2, 1, and 0, respectively. According to the Goodenough−Kanamori rules,[51] Fe^{3+}−Fe^{3+} superexchange interactions (e^1−O−e^1) are antiferromagnetic, Fe^{3+}−Mn^{3+} interactions (e^1−O−e^1 and e^1−O−e^0) antiferromagnetic and ferromagnetic, and Fe^{3+}−Mn^{4+} interactions (e^1−O−e^0) ferromagnetic. Hence, Removing e_g electrons by increasing x and δ yields fewer antiferromagnetic superexchange interactions and more frustrated antiferromagnetic order, accounting for the decreasing Néel temperature observed by DSC (see Figure 5). Experimentally, T_N scales with the average number of e_g electrons on the B site, as shown in Figure 13. Complex magnetic behavior at cryogenic temperatures is anticipated in materials with high x and/or δ, in analogy with $BiMnO_{3+\delta}$ and $LaMnO_{3+\delta}$.[16,52] Pure $BiFeO_3$ has been reported to display spin glass behavior and several low-temperature magnetic phase transitions;[47] however, hitherto, there are no reports on the influence of oxygen stoichiometry on the magnetic structure of Mn-substituted $BiFeO_3$ below room temperature. We note that the Néel transition is associated with a continuous, positive thermal expansion anomaly for $x = 0.0$ and 0.1, as evident from the inset in Figure 6. With increasing x, and more-frustrated antiferromagnetic order, thermal expansion anomalies associated with T_N could not be determined.

Solubility of Mn in $BiFeO_3$. The ambient pressure solubility limit of Mn in $BiFeO_3$ is clearly temperature-dependent, as evidenced from the different amounts of secondary phases revealed by XRD in Figure 8a. Because all the reflections from secondary phases could be indexed as $Bi_2Fe_{4-y}Mn_yO_{9+\delta'}$ (mullite) and $Bi_{25}Fe_{1-z}Mn_zO_{39+\delta''}$ (sillenite), adding Mn beyond the solubility limit shifts the reaction,[53,54]

$$\left(\frac{12}{49}\right)Bi_2Fe_{4-y}Mn_yO_{9+\delta'} + \left(\frac{1}{49}\right)Bi_{25}Fe_{1-z}Mn_zO_{39+\delta''} \rightleftarrows BiFe_{1-x}Mn_xO_{3+\delta} \quad (2)$$

toward the left-hand side. We have previously shown that increasing the temperature above 800 °C drives reaction 2 toward the right-hand side.[54] The Gibbs energy of reaction 2 is close to zero;[54] therefore, the influence of impurities is very important for the phase formation. Valant et al. have shown that adding impurities that are more soluble in the mullite or sillenite phase drives reaction 2 toward the left-hand side.[55]

Attempts to increase the solubility of Mn in $BiFeO_3$ by firing samples with $x > 0.3$ in a flowing O_2 atmosphere were unsuccessful, yielding a larger fraction of sillenite and mullite than in the samples fired in air shown in Figure 8a. Thus, Mn^{4+} is apparently more soluble in the mullite and sillenite phases than the perovskite phase, pointing to a higher tolerance of excess oxygen and cation vacancies in the former structures than the latter. This is supported by reports on $Bi_2Mn_4O_{10}$, possessing 50% Mn^{4+}.[56] The molar volume change of reaction 2 is large and negative, $\Delta_{r,(2)}V_m < 0$; thus, high pressure will favor formation of the perovskite phase.[54] The small Gibbs energy of reaction 2, and the large, negative $\Delta_{r,(2)}V_m$, are thermodynamic factors that explain why single-phase bulk $BiFe_{1-x}Mn_xO_{3+\delta}$ with $x > 0.3$ (e.g., $BiMnO_3$) are metastable and must be prepared via high-pressure synthesis. A theoretical study suggests that $BiFe_{0.5}Mn_{0.5}O_3$ has a positive enthalpy of formation, relative to $BiFeO_3$ and $BiMnO_3$ at 0 K,[57] implying that the enthalpy of solution is positive in the $BiFeO_3$−$BiMnO_3$ pseudo-binary system. This is consistent with increasing the solubility of manganese at higher temperatures, because the entropy of solution is positive.

Conductivity and Device Applications. Leakage currents due to high conductivity hampers the application of the ferroelectric polarization in $BiFeO_3$, and they are the probable origin of the low polarization found experimentally[4] in $BiFeO_3$ until the recent measurements on high-quality thin films, single crystals, and ceramics.[7] Although some reports find that small amounts of manganese doping reduces the conductivity of $BiFeO_3$,[58] other works point to an increasing conductivity with increasing manganese content,[59] which is

(50) (a) Thomas, N. W. *Acta Crystallogr., Sect. B: Struct. Sci.* **1996**, *52*, 954. (b) Avdeev, M.; Caspi, E. N.; Yakovlev, S. *Acta Crystallogr., Sect. B: Struct. Sci.* **2007**, *63*, 363.
(51) Goodenough, J. B. *Magnetism and the Chemical Bond*; John Wiley and Sons: New York, 1963.
(52) (a) Prado, F.; Sánchez, R. D.; Caneiro, A.; Causa, M. T.; Tovar, M. *J. Solid State Chem.* **1999**, *146*, 418. (b) Raj Sankar, C.; Joy, P. A. *Phys. Rev. B* **2005**, *72*, 132407. (c) De, K.; Ray, R.; Narayan Panda, R.; Giri, S.; Nakamura, H.; Kohara, T. *J. Magn. Magn. Mater.* **2005**, *288*, 339.
(53) Carvalho, T. T.; Tavares, P. B. *Mater. Lett.* **2008**, *62*, 3984.
(54) Selbach, S. M.; Einarsrud, M.-A.; Grande, T. *Chem. Mater.* **2009**, *21*, 169.
(55) Valant, M.; Axelsson, A.-K.; Alford, N. *Chem. Mater.* **2007**, *19*, 5431.
(56) Nguyen, N.; Legrain, M.; Ducouret, A.; Raveau, B. *J. Mater. Chem.* **1999**, *9*, 731.
(57) Bi, L.; Taussig, A. R.; Kim, H.-S.; Wang, L.; Dionne, G. F.; Bono, D.; Persson; Ceder, G.; Ross, C. A. *Phys. Rev. B* **2008**, *78*, 104106.
(58) (a) Singh, S. K.; Ishiwara, H.; Maruyama, K. *Appl. Phys. Lett.* **2006**, *88*, 262908. (b) Naganuma, H.; Miura, J.; Okamura, S. *Appl. Phys. Lett.* **2008**, *93*, 052901.
(59) (a) Chung, C.-F.; Lin, J.-P.; Wu, J.-M. *Appl. Phys. Lett.* **2006**, *88*, 242909. (b) Kharel, P.; Ramachandran, B.; Dixit, A.; Naik, V. M.; Sahana, M. B.; Sudakar, C.; Naik, R.; Rao, M. S. R.; Lawes, G. *J. Phys.: Condens. Matter.* **2009**, *21*, 036001. (c) Wen, Z.; Hu, G.; Fan, S.; Yang, C.; Wu, W.; Zhou, Y.; Chen, X.; Cui, S. *Thin Solid Films* **2009**, *517*, 4497.

consistent with our results in Figure 7. In a mixed valence system such as $BiFe_{1-x}Mn_xO_{3+\delta}$, polaron hopping is the commonly found mechanism of electrical conductivity at elevated temperatures.[60] We have previously shown that $BiFe_{0.7}Mn_{0.3}O_{3+\delta}$ is a *p*-type semiconductor; thus, the conductivity will increase as δ increases, according to eq 1.[14] Therefore, a stoichiometric oxygen content will increase the resistivity of the material. The possibility of controlling the conductivity of $BiFe_{1-x}Mn_xO_{3+\delta}$ by varying x and δ could have technological applications, e.g., in photovoltaic diodes or photocatalysts.[61]

The influence of x and δ on the lattice parameters could be important with respect to strained, epitaxial interfaces in thin films. Strain gradients can be accommodated by compositional gradients, and opposite effects are anticipated for substrates yielding compressive and tensile epitaxial strain. The different ionic radii of Mn^{3+} and Mn^{4+} opens the possibility of "chemical strain relaxation" by compositional gradients at epitaxial interfaces or in the vicinity of ferroelectric or ferroelastic domain walls. The latter have been shown to possess different conductivity than the bulk of ferroelastic domains for pure $BiFeO_3$.[62] Vacancies, and compensating change of cation valence, have also recently been shown to be important for strain relaxation at epitaxial interfaces of pure $BiFeO_3$ thin films.[63]

Understanding of the influence of x and δ on the structural and electrical properties of bulk $BiFe_{1-x}Mn_xO_{3+\delta}$ is important both to optimize the performance ferroelectric or multiferroic memories and to predict new technological applications of this material system.

(60) Karmakar, A.; Majumdar, S.; Giri, S. *Phys. Rev. B* **2008**, *79*, 094406.
(61) (a) Li, S.; Lin, Y.-H.; Zhang, B.-P.; Nan, C.-W.; Wang, Y. *J. Appl. Phys.* **2009**, *105*, 056105. (b) Choi, T.; Lee, S.; Choi, Y. J.; Kiryukhin, V.; Cheong, S.-W. *Science* **2009**, *324*, 63.
(62) Seidel, J.; Martin, L. W.; He, Q.; Zhan, Q.; Chu, Y.-H.; Rother, A.; Hawkridge, M. E.; Maksymovych, P.; Yu, P.; Gajek, M.; Balke, N.; Kalinin, S. V.; Gemming, S.; Wang, F.; Catalan, G.; Scott, J. F.; Spaldin, N. A.; Orenstein, J.; Ramesh, R. *Nat. Mater.* **2009**, *8*, 229.
(63) (a) Yuan, G. L.; Uedono, A. *Appl. Phys. Lett.* **2009**, *94*, 132905. (b) Yuan, G. L.; Martin, L. W.; Ramesh, R.; Uedono, A. *Appl. Phys. Lett.* **2009**, *95*, 012904.

Conclusions

The crystal structure of $BiFe_{1-x}Mn_xO_{3+\delta}$ shows systematic variations with x ($0.0 \leq x \leq 0.3$) and excess oxygen δ ($0.00 \leq \delta \leq 0.06$). Excess oxygen found from thermogravimetry is compensated by cation vacancies and partial oxidation of Mn^{3+} to Mn^{4+}.

The unit-cell volume and rhombohedral distortion decrease with increasing x and δ. This correlates with the decreasing ferroelectric Curie temperature (T_C) and the temperature of transition to the cubic state (T_{cub}), which both decrease with increasing x and δ. X-ray diffraction patterns and lattice strain from Rietveld refinement suggest that structural disorder caused by Mn substitution and excess oxygen is responsible for the decay of ferroelectricity with x and δ. The Néel temperature (T_N) decreases rapidly with x and δ, and this value is proposed to scale with the number of e_g electrons responsible for antiferromagnetic superexchange interactions.

The proposed phase diagram displays the stability regions of phases with three, two, one, and zero simultaneous ferroic orders. The solubility limit of Mn in $BiFe_{1-x}Mn_xO_{3+\delta}$ at ambient pressure is shown to be closely above $x = 0.3$, and it is shown to increase as the temperature increases. A thermodynamic explanation for the ambient pressure solid solubility limit is given, which also accounts for the formation of single-phase perovskite with $x > 0.3$ by high-pressure synthesis or epitaxial stabilization.

The electrical conductivity increases as the Mn substitution increases, while the apparent activation energy of conduction decreases. The present systematic study of the influence of x and δ on the conductivity and crystal structure of bulk $BiFe_{1-x}Mn_xO_{3+\delta}$ provides important insight to the effect of oxygen stoichiometry for technological applications of Mn-substituted $BiFeO_3$.

Acknowledgment. This work was supported by the Norwegian University of Science and Technology and the Research Council of Norway (NANOMAT, Grants 158518/431, 140553/I30, and 162874/V00).